


Propagation time and nondipole contributions to intraband high-order harmonic generation

Simon Vendelbo Bylling Jensen  and Lars Bojer Madsen *Department of Physics and Astronomy, Aarhus University, DK-8000 Aarhus C, Denmark* (Received 29 November 2021; accepted 26 January 2022; published 7 February 2022)

Applying the semiclassical model, we identify two connected effects in intraband high-order harmonic generation (HHG): (1) propagation time from the point of emission at the source to the point of detection, and (2) beyond-electric-dipole corrections to the light-matter interaction. These effects inherit information regarding the dispersion and cause specific features in the spectra including even-ordered harmonics in systems with space- and time-inversion symmetry. They can for certain experimental geometries be measured free of the dipole background.

DOI: [10.1103/PhysRevA.105.L021101](https://doi.org/10.1103/PhysRevA.105.L021101)

High-order harmonics (HHG) is a central part of strong-field and attosecond science due to its capability to produce ultrafast bursts of coherent ultraviolet light and to probe ultrafast electron dynamics [1–9]. HHG in gases can be rationalized by the three-step model, in which an atom is ionized, the continuum electron then propagates through the external field, and later recombines upon emission of its excess energy [10–12]. HHG within the diverse range of condensed-matter systems is widely debated [13–25], but for band-gap materials often described by intra- and interband dynamics. The interband process bears similarities to the three-step model [12], as the electron is excited to a conduction band, whereafter it propagates to later recombine with its hole and emit its excess energy [19]. For the intraband process, harmonics are generated as an electron wave packet propagates through a band dispersion that deviates from the quadratic free-electron one. Although both processes are coupled [19,26], generally the interband (intraband) mechanism dominates the HHG spectrum at harmonics beyond (below) the band gap.

With increasing significance in the long-wavelength regime [27], the intraband process described with a semiclassical model has been excellent for modeling a variety of HHG experiments. It has reproduced the characteristics of the spectrum and cutoff scaling of ZnO [28], orientation dependencies for MgO [25], orientation and polarization dependencies in GaSe [29], qualitative features of the spectra of ZnS [30], polarization and band-structure properties of ZnSe [31,32], qualitative dynamics of the Berry curvature for monolayer MoS₂ [33], spectral features and cutoff scaling for extreme ultraviolet beyond band-gap harmonics, as well as reconstructed the Berry curvature of SiO₂ [34,35]. In addition, the interpretation of the semiclassical model is intuitive, as it bears resemblance to the equations of motion for free electrons driven by electric and magnetic fields. However, for free electrons in a similar strong-field long-wavelength regime, a breakdown of the electric dipole approximation for the light-matter interaction occurs in a variety of processes (see, e.g., Refs. [36–44]). Beyond-dipole corrections are often associated with the high-frequency regime, and thus for

condensed-matter HHG, they have only been considered in the scope of examining the nondipole nature of the highest-frequency components of the emitted harmonic field [45]. An investigation of the validity of the dipole approximation within the low-frequency regime of the driving field seems crucial, as here the dipole approximation has been readily applied for the semiclassical approach in the literature [28–35]. Following this, identification of nondipole-induced features in the HHG spectra is critical in order to, e.g., distinguish them from topological features, which also arise in the semiclassical equations of motion [46]. Furthermore, since a nondipole radiation-pressure force typically arises in the high-intensity regime [47–49] it is relevant to reconsider the emitted radiation pattern since the emitter might be moving nontrivially towards or away from the detector.

A characteristic of the intraband process is that the harmonics are emitted throughout the electron trajectory and not simply upon recombination. It differs significantly from the interpretation of gaseous or interband HHG. For HHG in gases, the three-step model prescribes that only the contribution of the electron wave packet, which returns to the nucleus, will emit harmonics at the recombination step [10,12]. This happens as a part of the electron wave packet returns to spatially overlap with the nucleus to form a time-dependent dipole moment and generate stimulated emission. When describing the observed spectrum at a detector, the signal will not only consist of a single atom radiation pattern but will consist of the coherent sum of the radiation from many atoms in the gas. The observed HHG signal is thus restricted on constructive interference, which infers that HHG is emitted mostly in the propagation direction of the driving field. For an account of such macroscopic effects of gaseous HHG, see, e.g., Ref. [50]. As a result of macroscopic effects, additional information regarding the generation process can be gained by considering the temporal and spatial distribution of the emitted radiation. For HHG in gases, this can be applied to, e.g., differentiate between long and short trajectories of the generation process [51]. For the intraband generation process, the dynamics are widely different. Here, the

generation process is described from the point of view of Bloch states, which are spread in real space across many atomic sites. In the semiclassical model, a wave packet of Bloch electrons is propagated. This wave packet is spread across many lattice sites, however, localized when compared to the applied long-wavelength driving field. The current induced by such a wave packet thus accounts for the coherent motion of electron contributions across many lattice sites. Furthermore, the intraband process does not require the recombination step, making it intrinsically different from the gaseous case. In the intraband dynamics, the electron wave packet induces a current throughout its trajectory, which causes the emission of harmonics. We expect, based on this widely different nature of the generation process, that macroscopic effects of another nature arise for HHG in solids. Of such effects are the propagational time delay required for the emitted harmonics to reach the detector. The time delay depends on the instantaneous distance towards the detector for the wave packet along its trajectory. Propagation time delay is expected to be relevant for the material characteristics of thin samples where other propagation effects are reduced. Similar to the gaseous case, we expect that such propagation effects imprint an additional layer of information regarding the generation process onto the observed spectra. Propagation delay effects introduces new features in the HHG spectra, which are connected to the nondipole-induced ones. Here, we consider the following: (i) How does the variable propagation time delay from emission to observation of the harmonics affect the observed spectra? (ii) To what extent can nondipole effects alter the spectra? (iii) When are such effects important, and how are they related?

The semiclassical model for an electron wave packet describes the dynamics of intraband electrons centered at position \mathbf{r} with wave vector \mathbf{k} . We examine a system with space- and time-inversion symmetry where the magnetization and Berry curvature vanish [52], allowing us to single out the behavior stemming from propagation time and nondipole effects. The three-dimensional dispersion is expanded $\varepsilon(\mathbf{k}) = \frac{\hbar^2}{4a^2m_e} \{1 + \sum_n \sum_{i=\{x,y,z\}} c_{n,i} \cos(nk_i a)\}$ with material-dependent $c_{n,i}$ coefficients. Similar $\varepsilon(\mathbf{k})$'s are applied in the literature [13,27,28,30–35]. Parameters of a generalized zinc-based crystal are applied with $c_{m,i} = -0.95\delta_{m,1} - 0.05\delta_{m,3}$ and lattice spacing $a = 5.4 \text{ \AA}$ [30]. Typical band gaps for such zinc-based crystals are of 3–4 eV, corresponding to transitions with ~ 6 –7 harmonic orders of the applied carrier frequency. The dynamics of the intraband wave packet of charge $-e$, $e > 0$, are governed by

$$\hbar \dot{\mathbf{k}} = -e(\mathbf{E} + \dot{\mathbf{r}} \times \mathbf{B}) \quad \text{and} \quad \dot{\mathbf{r}} = \frac{1}{\hbar} \frac{\partial \varepsilon(\mathbf{k})}{\partial \mathbf{k}}, \quad (1)$$

where \mathbf{E} and \mathbf{B} are the space- and time-dependent electric and magnetic fields derived from the vector potential $\mathbf{A} = A_0(\eta)[0, \varepsilon \cos(\eta), \sin(\eta)]^T$ with $\eta = \omega t - \omega x/c$, where c is the speed of light. Throughout this work an angular frequency of $\omega = 0.0217 \text{ a.u.}$ ($\lambda = 2100 \text{ nm}$) is applied. $A_0(\eta)$ is a 30-cycle \sin^2 envelope function, and $\varepsilon \in [0; 1]$ describes the polarization, with $\varepsilon = 0$ and $\varepsilon = 1$ for linearly and circularly polarized light, respectively. To retain an intensity of $I = 5.3 \times 10^{11} \text{ W/cm}^2$ when varying ε , the amplitude of the vector potential in atomic

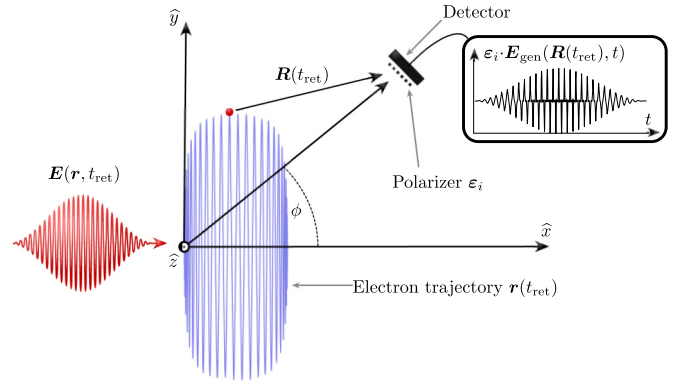


FIG. 1. Illustration of the electron dynamics in retarded time. The incoming electric field $\mathbf{E}(\mathbf{r}, t_{\text{ret}})$, illustrated as circularly polarized in the (y, z) plane and propagating in the x direction, induces an electron wave-packet trajectory, which is magnified in the figure. Relative to this trajectory, the detector position is noted $\mathbf{R}(t_{\text{ret}})$ and depends on the retarded emission time t_{ret} . After the propagational delay between t_{ret} and the detection time t , the detector, placed at angle ϕ in the (x, y) plane, measures the spectrum of the generated field $\mathbf{E}_{\text{gen}}(\mathbf{R}(t_{\text{ret}}), t)$ with an associated polarizer singling out ε_i -polarized harmonics.

units is scaled as $A_0 = \sqrt{I}/(\omega\sqrt{1 + \varepsilon^2})$. When considering nondipole effects within the strong-field, long-wavelength limit, it is useful to expand the vector potential as $\mathbf{A} = \sum_{l=0}^{\infty} \mathbf{A}^{(l)}$ with $\mathbf{A}^{(l)}$ denoting the l th order of $\omega x/c$ such that $\mathbf{A}^{(l)} = (l!)^{-1} d^l \mathbf{A}/d\eta^l |_{\eta=\omega t} (-\omega x/c)^l$. The electric and magnetic fields inherit the notation of the associated $\mathbf{A}^{(l)}$, such that $\mathbf{E}^{(l)} = -\partial_t \mathbf{A}^{(l)}$ and $\mathbf{B}^{(l)} = \nabla \times \mathbf{A}^{(l)}$. Thereby $\mathbf{A}^{(0)}$ is the term within the commonly applied electric dipole approximation, in which the term $q\dot{\mathbf{r}} \times \mathbf{B}$ of Eq. (1) vanishes as $\mathbf{B}^{(0)} = \mathbf{0}$.

Phase-matching effects modify HHG in solids similar to introducing a rapid dephasing and can be neglected for thin targets in the detection direction [53]. Doing so, the acceleration electric field emitted by the electronic wave packet, observed at $\mathbf{R}(t_{\text{ret}})$, is [54]

$$\mathbf{E}_{\text{gen}}(\mathbf{R}(t_{\text{ret}}), t) = -\frac{e\mathbf{R}(t_{\text{ret}}) \times [\mathbf{R}(t_{\text{ret}}) \times \ddot{\mathbf{r}}(t_{\text{ret}})]}{4\pi\epsilon_0 c^2 R(t_{\text{ret}})^3}. \quad (2)$$

For an illustration of the geometry, see Fig. 1. Effects arising due to the focal spot size are not included and are expected to be negligible in experimental geometries where variations of the distance towards the detector are negligible across the width of the focal spot. With increasing ϕ (Fig. 1) this could be maintained by engineering or angling the sample. The harmonics generated at the retarded emission time t_{ret} are observed at the detection time $t = t_{\text{ret}} + R(t_{\text{ret}})/c$ after the propagation time delay $R(t_{\text{ret}})/c$. The electron trajectory is therefore evaluated at the retarded time. Typically for HHG in solids, an approximation to this formula is applied, in which one neglects the propagational time delay, i.e., the difference between the time of emission t_{ret} and the time of detection t . In doing so, the emitted spectra are derived from the current $\mathbf{j}(t)$ or the time derivative hereof, which for the case of a localized electronic wave packet can be written as

$$\mathbf{E}_{\text{gen},0}(t) \propto -\frac{d\mathbf{j}(t)}{dt} = e\dot{\mathbf{r}}(t). \quad (3)$$

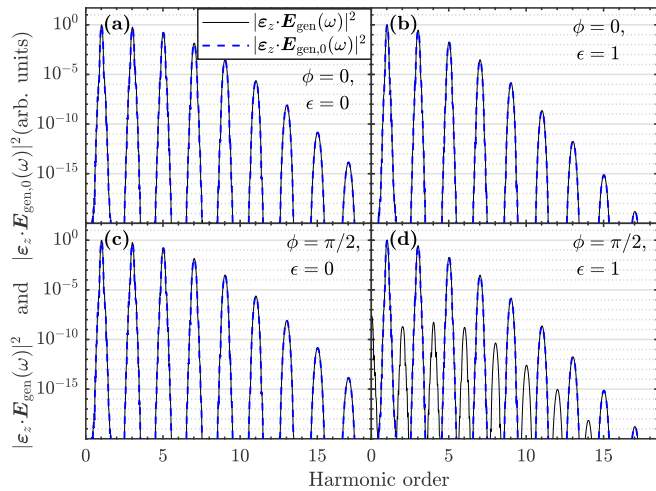


FIG. 2. Calculated \mathbf{e}_z -polarized HHG spectra observed at $\phi = 0$ (see Fig. 1) with (a) linearly polarized and (b) circularly polarized driving fields. Similar spectra are given with $\phi = \pi/2$ for (c) and (d), respectively. The radiation pattern $|E_{\text{gen}}(\omega)|^2$ from Eq. (2) (black continuous) is compared to the approximation $|E_{\text{gen},0}(\omega)|^2$ of Eq. (3) (blue dashed) induced by an intraband electronic wave packet with initial conditions $\mathbf{r} = [0, 0, 0]^T$ and $\mathbf{k} = [0, 0, 0]^T$. See text for laser parameters.

In general, we consider a detector placed at an angle ϕ in the (x, y) plane measuring \mathbf{e}_i -polarized light at a distance of 1 m from the origin of the electronic wave packet (Fig. 1). We have checked that the results of the present work are independent of changes to the macroscopic distance $R(t = 0)$ to fit specific experimental setups. For the numerical simulation, we initialize an electron wave packet at the Γ point, $\mathbf{k}(t = 0) = [0, 0, 0]^T$ and $\mathbf{r}(t = 0) = [0, 0, 0]^T$, as is typically done within the literature [30,31,34,35]. The model does not account for field-induced electron correlation effects, which is justified when applying a single driving pulse [55]. The electron wave packet is propagated through Eq. (1), beyond and within the dipole approximation.

First, in Fig. 2, we investigate solely the propagation time delay effect. To this end, we consider a regime where nondipole effects are shown later to be negligible, namely by considering \mathbf{e}_z -polarized harmonics originating dominantly from the z -polarized current within the polarization plane. In Fig. 2, we compare the predictions of Eq. (2) with those of the approximate Eq. (3), for a linearly and circularly polarized field with detector positions $\phi = \{0, \pi/2\}$. Figure 2(a) shows that the approximation of Eq. (3) is justified at $\phi = 0$. The reason is that the temporal variation in $R(t_{\text{ret}})$ is relatively small when the detector is placed perpendicular to the polarization direction of the driving field. In Fig. 2(b) the electron dynamics is no longer one dimensional, as the wave packet is driven in the polarization (y, z) plane of the circularly polarized driving field. Since, however, the detector is placed in a direction perpendicular to this plane, Eq. (3) is still accurate. Comparing Figs. 2(a) and 2(b), we note that a reduction is found in the spectra with increasing ellipticity, due to the amplitude of the electric vector potential decreasing for fixed intensity. The electron driven linearly in the z

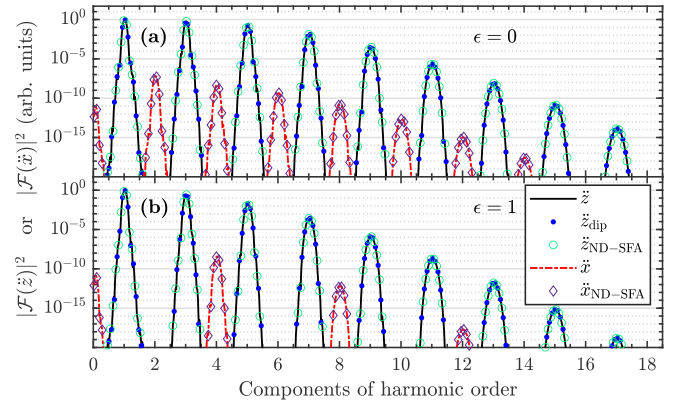


FIG. 3. Norm square of the Fourier transform of the acceleration along the polarization \hat{z} or propagation \hat{x} direction for a driving field with (a) linear $\epsilon = 0$ and (b) circular $\epsilon = 1$ polarization. The acceleration induced by the electromagnetic field is compared to that induced by the dipole field and the ND-SFA approach of Eq. (4). For the propagation direction, the acceleration obtained within the dipole approximation vanishes. The parameters are as in Fig. 2.

direction will dominantly emit a symmetrical radiation pattern in the (x, y) plane, as prescribed by the dipole radiation pattern. This is seen when comparing different ϕ in Figs. 2(a) and 2(c), which are normalized by identical scaling. For the circularly polarized driving field, however, this symmetry is broken by propagation time delay as observed in Fig. 2(d). For finite ϕ the electron has an excursion in the direction of the detector, causing a relatively larger change in the distance to the detector $R(t_{\text{ret}})$, and a time-dependent propagation delay (Fig. 1). This effect infers that an electron accelerating with a given frequency $l\omega$ will be observed to attain additional frequency components of $(l \pm 1)\omega$. In Fig. 2(d) this is apparent as even harmonics arise with intensity scaling as $\sin^2(\phi)$. Propagation delay effects can seemingly be neglected in Figs. 2(a)–2(c), where the electron trajectory is confined to a plane perpendicular to the direction towards the detector and the effect of the variations of the propagational delay is of higher order. Oppositely such effects must be included if the detector occupies a solid angle with multiple ϕ components, or if a significant excursion of the wave packet is in the direction of the detector, where it generates additional side peaks in the spectra. The magnitude of such side peaks depends on the electron trajectory, and can thus bring insight into properties of the material. We note that these results are qualitatively similar to those obtained by initializing the electron wave packet at the driving field maxima, where the excitation process is most likely (see Supplemental Material [56]).

We now analyze nondipole effects in Fig. 3. In order to single these out from the propagation delay effects, we start by analyzing the acceleration of the electron wave packet to characterize the nondipole components hereof. Later the nondipole effects on the HHG spectrum will be examined inserting the acceleration in Eq. (2). In regions where Eq. (3) is accurate, we can draw conclusions based on the frequency components of the wave-packet acceleration. To investigate the nondipole corrections to the electron acceleration we include leading-order effects from the interaction between the

dipole-induced motion and the magnetic field. A similar approach was found to account for nondipole effects in atomic systems [49,57,58]. In this nondipole strong-field approximation (ND-SFA) approach, the first part of Eq. (1) reduces to

$$\hbar\dot{\mathbf{k}} = -e[(-\partial_t A^{(0)}) + (\dot{r}_y B_z^{(1)} - \dot{r}_z B_y^{(1)})\hat{x}], \quad (4)$$

where the last term describes a radiation-pressure-like force on the wave packet in the laser propagation direction [49]. Simulations with the fully retarded, the ND-SFA, and the dipole field are compared in Fig. 3. For the acceleration within the polarization plane [\ddot{z} in Figs. 3(a) and 3(b)] the dynamics are well described within the dipole approximation, consistent with the free-electron case [49]. Also, similar to the free-electron case, significant nondipole corrections arise for the dynamics in the propagation direction in Figs. 3(a) and 3(b) where a harmonic nondipole acceleration containing

$$\ddot{r} = \frac{\hbar\omega}{2am_e} \sum_n \sum_{l=1,3,5,\dots}^{\infty} \left[\begin{array}{l} -\frac{\hbar(l+1)}{am^*c} \{c_{n,z} J_{l+1}[\frac{nae}{\hbar} A_0(\omega t)] + c_{n,y} (-1)^{(l+1)/2} J_{l+1}[\frac{nae}{\hbar} \epsilon A_0(\omega t)]\} \sin[(l+1)\omega t] \\ nl c_{n,y} (-1)^{(l-1)/2} J_l[\frac{nae}{\hbar} \epsilon A_0(\omega t)] \sin(l\omega t) \\ -nl c_{n,z} J_l[\frac{nae}{\hbar} A_0(\omega t)] \cos(l\omega t) \end{array} \right], \quad (5)$$

where J_l are Bessel functions and m^* is the effective mass of the dispersion along the propagation direction [56]. We note that the arguments of the Bessel functions in the long-pulse limit can be expressed in terms of ω_B/ω with $\omega_B = eaA_0\omega/\hbar$ the Bloch frequency. The analytical approach accurately describes the dominant nondipole dynamics, and allows for characterizing the selection rules for the harmonic contributions to the acceleration [56]. Generally, with space- and time-inversion symmetry only odd- (even-) frequency components will be present in the y and z direction (x direction), respectively [56]. Furthermore, for a circularly polarized driving field and if the dispersion in both directions of the polarization plane is identical, $c_{n,y} = c_{n,z}$, then the x direction will consist of only fourth-ordered harmonic motion [56], similar to what is observed in Fig. 3(b). The detection of the nondipole acceleration thus provides a tool to investigate the symmetries of the material at hand as well as the dispersion along both the propagation and polarization directions.

Lastly, we consider in Fig. 4 the interplay between the propagation time and nondipole effects. In general, the two mechanisms couple since nondipole corrections to the electron trajectory modify $\mathbf{R}(t_{\text{ret}})$ of Eq. (2) altering the propagation time delay $R(t_{\text{ret}})/c$. Furthermore, the nondipole ϵ_z -polarized harmonics are sensitive to propagation time delay as they are observed at nonvanishing ϕ . We consider a detector placed at $\phi = \pi/2$ since here both the emitted HHG spectra of the electron acceleration from the polarization plane and from the nondipole x motion can be observed by considering the ϵ_z - and ϵ_x -polarized harmonics, respectively. The HHG spectra, calculated from Eq. (2), are given in Fig. 4. At first, when comparing Figs. 3(a) and 4(a), no significant propagation delay effects are observed. This is due to the nondipole-induced dynamics along the propagation direction being of order $1/c$ lower than the excursion in the polarization plane. Similarly, no nondipole effects were found for the spectra of Figs. 2(a) and 2(c). For circularly polarized

even-ordered multiples of the driving frequency is observed. Remarkably for circularly polarized light, in Fig. 3(b), only nondipole effects of fourth-order multiples are observed. In the long-pulse circularly polarized driving-field regime, a free electron would have $\dot{r}_y \propto A_y^{(0)}$ and $\dot{r}_z \propto A_z^{(0)}$, in which case the last term of Eq. (4) vanishes, as $\mathbf{A}^{(0)} \parallel \mathbf{B}^{(1)}$ [49]. This is not the case for the intraband wave packet as its induced velocity in the polarization plane is not proportional to $\mathbf{A}^{(0)}$, but modified by the nonparabolic band dispersion as captured by the last part of Eq. (1). These predictions solidify the different nature of nondipole effects for atomic or intraband dynamics. We observe in Fig. 3 that the ND-SFA approach accurately describes these dynamics. Due to its simplicity, it is suitable for analytical calculations (see Supplemental Material [56]) in which one can find the wave-packet acceleration to be

light, the excursion in the y direction of the polarization plane contributes with additional side peaks to Fig. 4(b), when compared to Fig. 3(b), for both the ϵ_z -polarized and the nondipole ϵ_x -polarized harmonics. Interestingly for the fourth harmonic in Fig. 4(b), the propagation time delay side peak from the ϵ_z -polarized harmonics is of similar magnitude as the dominant nondipole harmonic with ϵ_x polarization. The interplay of nondipole effects and propagation delay effects can thus be investigated by considering the ellipticity dependence of specific harmonics as a function of ϕ and the signatures of each mechanism can be readily distinguished in experiments by varying the detector angle ϕ and observed polarization ϵ_i . If observing ϵ_x -polarized harmonics at $\phi = \pi/2$, nondipole harmonics can be identified free of the vanishing background of harmonics emitted within the dipole approximation. Both propagation time and nondipole effects can thus be singled out by varying the driving field ellipticity and detection angle. Features arising in the HHG spectra from both mechanisms

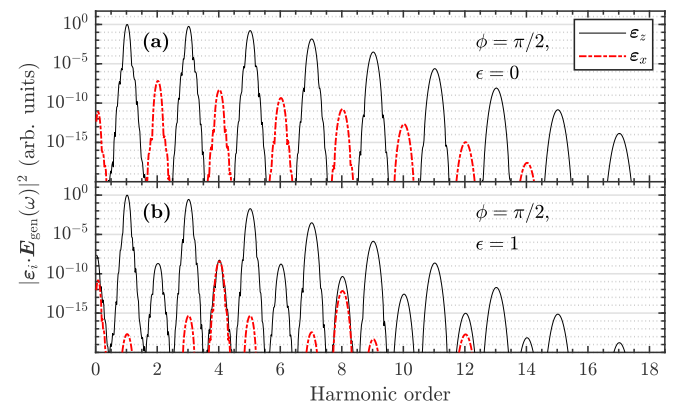


FIG. 4. HHG spectra, $|\epsilon_i \cdot \mathbf{E}_{\text{gen}}(\omega)|^2$, including polarization time delay in Eq. (2) for the \ddot{z} and \ddot{x} accelerations in Fig. 3. The detector is placed at an angle of $\phi = \pi/2$.

carry information about the dispersion both within the polarization and propagation directions. Similarly, the nondipole harmonics are sensitive to the symmetry of the sample, as discussed in relation to Fig. 3, and therefore in principle provide a path to examining structural changes on an ultrafast timescale. We also note that the significance of nondipole harmonics, as well as propagation time delay contributions, is restricted by the effective mass of the system [see Eq. (5)], and is expected to increase with a lower effective mass, where also the harmonic cutoff is expected to be extended [26,59,60]. Furthermore, both effects are expected to increase in magnitude in the regime of low-frequency, high-intensity driving fields. A detailed investigation onto such other materials and parameter regimes is a topic for future work. If initializing the electron wave packet at the driving field maxima, the results of Figs. 3 and 4 remain qualitatively identical for a linearly polarized driving field. For circularly polarized light the broken time-reversal symmetry can affect the spectra (see Supplemental Material [56]).

In conclusion, by including propagation time delay to intraband HHG, additional side peaks appear in the HHG spectra, resulting in even harmonics despite space- and time-inversion symmetries in the sample. The propagation delay depends on

the position of the detector compared to the emitting electron wave packet, and the effect is negligible if the wave packet is having a relatively small amplitude motion in the direction towards the detector. We have characterized nondipole corrections to the electron wave-packet dynamics as an oscillatory motion in the propagation direction of the driving field. By analyzing a leading-order approximation to the equation of motion, we provide an analytical assessment of the nondipole effects [Eq. (5)]. For inversion symmetric lattices, selection rules are found for the emitted nondipole harmonics. These are even- or fourth-ordered for the case of a linearly or circularly polarized driving field. For a complete description of the HHG process, one must be aware of the interplay of propagation time and nondipole effects. Both effects bring information regarding material properties, which affect the real-space electronic trajectory and velocity. Similarly, they provide a tool for investigating the symmetries of the sample and reconstructing the dispersion both within and out of the polarization plane.

We thank Stefano M. Cavaletto for useful suggestions. This work was supported by the Danish Council for Independent Research (Grant No. 9040-00001B).

-
- [1] M. Lein, N. Hay, R. Velotta, J. P. Marangos, and P. L. Knight, Interference effects in high-order harmonic generation with molecules, *Phys. Rev. A* **66**, 023805 (2002).
- [2] R. Torres, N. Kajumba, J. G. Underwood, J. S. Robinson, S. Baker, J. W. G. Tisch, R. de Nalda, W. A. Bryan, R. Velotta, C. Altucci, I. C. E. Turcu, and J. P. Marangos, Probing Orbital Structure of Polyatomic Molecules by High-Order Harmonic Generation, *Phys. Rev. Lett.* **98**, 203007 (2007).
- [3] W. Li, X. Zhou, R. Lock, S. Patchkovskii, A. Stolow, H. C. Kapteyn, and M. M. Murnane, Time-resolved dynamics in N₂O₄ probed using high harmonic generation, *Science* **322**, 1207 (2008).
- [4] S. Baker, J. S. Robinson, C. A. Haworth, H. Teng, R. A. Smith, C. C. Chirilă, M. Lein, J. W. G. Tisch, and J. P. Marangos, Probing proton dynamics in molecules on an attosecond time scale, *Science* **312**, 424 (2006).
- [5] M. Lein, Attosecond Probing of Vibrational Dynamics with High-Harmonic Generation, *Phys. Rev. Lett.* **94**, 053004 (2005).
- [6] J. Itatani, J. Levesque, D. Zeidler, H. Niikura, H. Pépin, J. C. Kieffer, P. B. Corkum, and D. M. Villeneuve, Tomographic imaging of molecular orbitals, *Nature (London)* **432**, 867 (2004).
- [7] O. Schubert, M. Hohenleutner, F. Langer, B. Urbaneck, C. Lange, U. Huttner, D. Golde, T. Meier, M. Kira, S. W. Koch, and R. Huber, Sub-cycle control of terahertz high-harmonic generation by dynamical Bloch oscillations, *Nat. Photonics* **8**, 119 (2014).
- [8] M. Garg, H. Y. Kim, and E. Goulielmakis, Ultimate waveform reproducibility of extreme-ultraviolet pulses by high-harmonic generation in quartz, *Nat. Photonics* **12**, 291 (2018).
- [9] G. Vampa, T. J. Hammond, N. Thiré, B. E. Schmidt, F. Légaré, C. R. McDonald, T. Brabec, D. D. Klug, and P. B. Corkum, All-Optical Reconstruction of Crystal Band Structure, *Phys. Rev. Lett.* **115**, 193603 (2015).
- [10] J. L. Krause, K. J. Schafer, and K. C. Kulander, High-Order Harmonic Generation from Atoms and Ions in the High Intensity Regime, *Phys. Rev. Lett.* **68**, 3535 (1992).
- [11] M. Lewenstein, P. Balcou, M. Y. Ivanov, A. L'Huillier, and P. B. Corkum, Theory of high-harmonic generation by low-frequency laser fields, *Phys. Rev. A* **49**, 2117 (1994).
- [12] P. B. Corkum, Plasma Perspective on Strong Field Multiphoton Ionization, *Phys. Rev. Lett.* **71**, 1994 (1993).
- [13] S. Ghimire, A. D. DiChiara, E. Sistrunk, G. Ndabashimiye, U. B. Szafuga, A. Mohammad, P. Agostini, L. F. DiMauro, and D. A. Reis, Generation and propagation of high-order harmonics in crystals, *Phys. Rev. A* **85**, 043836 (2012).
- [14] P. G. Hawkins, M. Y. Ivanov, and V. S. Yakovlev, Effect of multiple conduction bands on high-harmonic emission from dielectrics, *Phys. Rev. A* **91**, 013405 (2015).
- [15] H. Lakhotia, H. Y. Kim, M. Zhan, S. Hu, S. Meng, and E. Goulielmakis, Laser picoscopy of valence electrons in solids, *Nature (London)* **583**, 55 (2020).
- [16] L. Yue and M. B. Gaarde, Structure gauges and laser gauges for the semiconductor Bloch equations in high-order harmonic generation in solids, *Phys. Rev. A* **101**, 053411 (2020).
- [17] L. Yue and M. B. Gaarde, Imperfect Recollisions in High-Harmonic Generation in Solids, *Phys. Rev. Lett.* **124**, 153204 (2020).
- [18] T. Tamaya, A. Ishikawa, T. Ogawa, and K. Tanaka, Diabatic Mechanisms of Higher-Order Harmonic Generation in Solid-

- State Materials Under High-Intensity Electric Fields, *Phys. Rev. Lett.* **116**, 016601 (2016).
- [19] G. Vampa, C. R. McDonald, G. Orlando, D. D. Klug, P. B. Corkum, and T. Brabec, Theoretical Analysis of High-Harmonic Generation in Solids, *Phys. Rev. Lett.* **113**, 073901 (2014).
- [20] T. Higuchi, M. I. Stockman, and P. Hommelhoff, Strong-Field Perspective on High-Harmonic Radiation from Bulk Solids, *Phys. Rev. Lett.* **113**, 213901 (2014).
- [21] T. Ikemachi, Y. Shinohara, T. Sato, J. Yumoto, M. Kuwata-Gonokami, and K. L. Ishikawa, Trajectory analysis of high-order-harmonic generation from periodic crystals, *Phys. Rev. A* **95**, 043416 (2017).
- [22] L. Li, P. Lan, X. Zhu, T. Huang, Q. Zhang, M. Lein, and P. Lu, Reciprocal-Space-Trajectory Perspective on High-Harmonic Generation in Solids, *Phys. Rev. Lett.* **122**, 193901 (2019).
- [23] M. Hohenleutner, F. Langer, O. Schubert, M. Knorr, U. Huttner, S. W. Koch, M. Kira, and R. Huber, Real-time observation of interfering crystal electrons in high-harmonic generation, *Nature (London)* **523**, 572 (2015).
- [24] M. Wu, D. A. Browne, K. J. Schafer, and M. B. Gaarde, Multilevel perspective on high-order harmonic generation in solids, *Phys. Rev. A* **94**, 063403 (2016).
- [25] Y. S. You, D. A. Reis, and S. Ghimire, Anisotropic high-harmonic generation in bulk crystals, *Nat. Phys.* **13**, 345 (2017).
- [26] D. Golde, T. Meier, and S. W. Koch, High harmonics generated in semiconductor nanostructures by the coupled dynamics of optical inter- and intraband excitations, *Phys. Rev. B* **77**, 075330 (2008).
- [27] G. Vampa, C. R. McDonald, G. Orlando, P. B. Corkum, and T. Brabec, Semiclassical analysis of high harmonic generation in bulk crystals, *Phys. Rev. B* **91**, 064302 (2015).
- [28] S. Ghimire, A. D. DiChiara, E. Sistrunk, P. Agostini, L. F. DiMauro, and D. A. Reis, Observation of high-order harmonic generation in a bulk crystal, *Nat. Phys.* **7**, 138 (2011).
- [29] K. Kaneshima, Y. Shinohara, K. Takeuchi, N. Ishii, K. Imasaka, T. Kaji, S. Ashihara, K. L. Ishikawa, and J. Itatani, Polarization-Resolved Study of High Harmonics from Bulk Semiconductors, *Phys. Rev. Lett.* **120**, 243903 (2018).
- [30] N. Klemke, O. D. Mücke, A. Rubio, F. X. Kärtner, and N. Tancogne-Dejean, Role of intraband dynamics in the generation of circularly polarized high harmonics from solids, *Phys. Rev. B* **102**, 104308 (2020).
- [31] A. A. Lanin, E. A. Stepanov, A. B. Fedotov, and A. M. Zheltikov, Mapping the electron band structure by intraband high-harmonic generation in solids, *Optica* **4**, 516 (2017).
- [32] A. A. Lanin, E. A. Stepanov, A. V. Mitrofanov, D. A. Sidorov-Biryukov, A. B. Fedotov, and A. M. Zheltikov, High-order harmonic analysis of anisotropic petahertz photocurrents in solids, *Opt. Lett.* **44**, 1888 (2019).
- [33] H. Liu, Y. Li, Y. S. You, S. Ghimire, T. F. Heinz, and D. A. Reis, High-harmonic generation from an atomically thin semiconductor, *Nat. Phys.* **13**, 262 (2017).
- [34] T. T. Luu, M. Garg, S. Y. Kruchinin, A. Moulet, M. T. Hassan, and E. Goulielmakis, Extreme ultraviolet high-harmonic spectroscopy of solids, *Nature (London)* **521**, 498 (2015).
- [35] T. T. Luu and H. J. Wörner, Measurement of the Berry curvature of solids using high-harmonic spectroscopy, *Nat. Commun.* **9**, 916 (2018).
- [36] A. Ludwig, J. Maurer, B. W. Mayer, C. R. Phillips, L. Gallmann, and U. Keller, Breakdown of the Dipole Approximation in Strong-Field Ionization, *Phys. Rev. Lett.* **113**, 243001 (2014).
- [37] B. Willenberg, J. Maurer, B. W. Mayer, and U. Keller, Sub-cycle time resolution of multi-photon momentum transfer in strong-field ionization, *Nat. Commun.* **10**, 5548 (2019).
- [38] N. Haram, I. Ivanov, H. Xu, K. T. Kim, A. Atia-tul Noor, U. S. Sainadh, R. D. Glover, D. Chetty, I. V. Litvinyuk, and R. T. Sang, Relativistic Nondipole Effects in Strong-Field Atomic Ionization at Moderate Intensities, *Phys. Rev. Lett.* **123**, 093201 (2019).
- [39] A. Hartung, S. Brennecke, K. Lin, D. Trabert, K. Fehre, J. Rist, M. S. Schöffler, T. Jahnke, L. P. H. Schmidt, M. Kunitski, M. Lein, R. Dörner, and S. Eckart, Electric Nondipole Effect in Strong-Field Ionization, *Phys. Rev. Lett.* **126**, 053202 (2021).
- [40] C. T. L. Smeenk, L. Arissian, B. Zhou, A. Mysyrowicz, D. M. Villeneuve, A. Staudte, and P. B. Corkum, Partitioning of the Linear Photon Momentum in Multiphoton Ionization, *Phys. Rev. Lett.* **106**, 193002 (2011).
- [41] A. Hartung, S. Eckart, S. Brennecke, J. Rist, D. Trabert, K. Fehre, M. Richter, H. Sann, S. Zeller, K. Henrichs, G. Kastirke, J. Hoehl, A. Kalinin, M. S. Schöffler, T. Jahnke, L. P. H. Schmidt, M. Lein, M. Kunitski, and R. Dörner, Magnetic fields alter strong-field ionization, *Nat. Phys.* **15**, 1222 (2019).
- [42] M.-X. Wang, S.-G. Chen, H. Liang, and L.-Y. Peng, Review on non-dipole effects in ionization and harmonic generation of atoms and molecules, *Chin. Phys. B* **29**, 013302 (2020).
- [43] N. Haram, R. T. Sang, and I. V. Litvinyuk, Transverse electron momentum distributions in strong-field ionization: Nondipole and Coulomb focusing effects, *J. Phys. B* **53**, 154005 (2020).
- [44] J. Maurer and U. Keller, Ionization in intense laser fields beyond the electric dipole approximation: concepts, methods, achievements and future directions, *J. Phys. B* **54**, 094001 (2021).
- [45] A. Gorlach, O. Neufeld, N. Rivera, O. Cohen, and I. Kaminer, The quantum-optical nature of high harmonic generation, *Nat. Commun.* **11**, 4598 (2020).
- [46] R. E. F. Silva, Á. Jiménez-Galán, B. Amorim, O. Smirnova, and M. Ivanov, Topological strong-field physics on sub-laser-cycle timescale, *Nat. Photonics* **13**, 849 (2019).
- [47] A. Bugacov, M. Pont, and R. Shakeshaft, Possibility of breakdown of atomic stabilization in an intense high-frequency field, *Phys. Rev. A* **48**, R4027(R) (1993).
- [48] J. R. Vázquez de Aldana, N. J. Kylstra, L. Roso, P. L. Knight, A. Patel, and R. A. Worthington, Atoms interacting with intense, high-frequency laser pulses: Effect of the magnetic-field component on atomic stabilization, *Phys. Rev. A* **64**, 013411 (2001).
- [49] S. V. B. Jensen, M. M. Lund, and L. B. Madsen, Nondipole strong-field-approximation Hamiltonian, *Phys. Rev. A* **101**, 043408 (2020).
- [50] M. B. Gaarde, J. L. Tate, and K. J. Schafer, Macroscopic aspects of attosecond pulse generation, *J. Phys. B* **41**, 132001 (2008).
- [51] M. Bellini, C. Lyngå, A. Tozzi, M. B. Gaarde, T. W. Hänsch, A. L'Huillier, and C.-G. Wahlström, Temporal Coherence of Ultrashort High-Order Harmonic Pulses, *Phys. Rev. Lett.* **81**, 297 (1998).
- [52] G. Sundaram and Q. Niu, Wave-packet dynamics in slowly perturbed crystals: Gradient corrections and Berry-phase effects, *Phys. Rev. B* **59**, 14915 (1999).

- [53] I. Kilen, M. Kolesik, J. Hader, J. V. Moloney, U. Huttner, M. K. Hagen, and S. W. Koch, Propagation Induced Dephasing in Semiconductor High-Harmonic Generation, *Phys. Rev. Lett.* **125**, 083901 (2020).
- [54] J. D. Jackson, *Classical Electrodynamics*, 3rd ed. (Wiley, New York, 1998).
- [55] S. V. B. Jensen and L. B. Madsen, Edge-state and bulklike laser-induced correlation effects in high-harmonic generation from a linear chain, *Phys. Rev. B* **104**, 054309 (2021).
- [56] See Supplemental Material at <http://link.aps.org/supplemental/10.1103/PhysRevA.105.L021101> for an analytical solution to the nondipole strong-field approximation equations of motion and a discussion on the initial conditions.
- [57] S. V. B. Jensen and L. B. Madsen, Nondipole effects in laser-assisted electron scattering, *J. Phys. B* **53**, 195602 (2020).
- [58] M. M. Lund and L. B. Madsen, Nondipole photoelectron momentum shifts in strong-field ionization with mid-infrared laser pulses of long duration, *J. Phys. B* **54**, 165602 (2021).
- [59] O. D. Mücke, Isolated high-order harmonics pulse from two-color-driven Bloch oscillations in bulk semiconductors, *Phys. Rev. B* **84**, 081202(R) (2011).
- [60] D. Golde, M. Kira, T. Meier, and S. W. Koch, Microscopic theory of the extremely nonlinear terahertz response of semiconductors, *Phys. Status Solidi B* **248**, 863 (2011).